A Dissipative Particle Dynamics Model for Thixotropic Materials Exhibiting Pseudo-yield Stress Behaviour☆

K. Le-Cao[1], N. Phan-Thien[1], B. C. Khoo[1], N. Mai-Duy[2]

Abstract

Many materials (e.g., gels, colloids, concentrated cohesive sediments, etc.) exhibit a stable solid form at rest, and liquify once subjected to an applied stress exceeding a critical value – a yield-stress behaviour. This can be qualitatively explained by the forming and destruction of the fluid microstructure [1], and it may be modelled as a thixotropic and yield stress material. In this paper, we propose a mesoscopic model which is able to mimic a thixotropic and yield stress behaviour using a particle-based technique known as dissipative particle dynamics (DPD). The DPD technique satisfies conservation of mass and momentum and it has been applied successfully for a number of problems involving complex-structure fluids, such as polymer solutions, suspensions of rigid particles, droplets, biological fluids, etc. In this work, an indirect linkage dissipative particle model (ILDP) is proposed based on qualitative microstructural physics, which results in a non-Newtonian fluid with observed yield stress and thixotropic properties. The model comprises of two types, or species, of DPD particles – with only repulsive conservative force between the same species, and with repulsive force at short range and attractive force at long range between different species. Numerical results show that the proposed DPD fluid can represent some observed complex behaviours, such as yield stress and thixotropic

☆

*Corresponding author

Email address: nhan@nus.edu.sg (N. Phan-Thien)

[1]Department of Mechanical Engineering, Faculty of Engineering, National University of Singapore, Singapore.

[2]Computational Engineering and Science Research Centre, School of Mechanical and Electrical Engineering,University of Southern Queensland, Toowoomba, QLD 4350, Australia.

effects.

Keywords: dissipative particle dynamics, DPD, Bingham model, yield stress, thixotropy

2010 MSC: 00-01, 99-00

1. Introduction

Many engineering flow processes involve complex structure liquids, for examples, foodstuffs, polymers, cosmetic products, crude oil, cohesive sediment mixtures, etc. Such complex liquids hardly flow if the applied load is lower than a certain value, but they are liquefied and flow easily at loading higher than this value. This critical stress threshold associated with this loading is called the "yield stress", and there are experimental evidences that these fluids do flow in a very viscous manner at a stress level lower than the yield stress, thus supporting modelling of the true fluid-to-solid transition by a very viscous transition at low strain rates. Moreover, the fluid at this low stress level is thixotropic as well; we refer the reader to an excellent recent review by Bonn [2] on this topic. The current view of this research area, which we share, of the yield stress as a very viscous transition remains an attractive and useful engineering idea, and that it is a result of a network microstructure generated by inter-particle interactions, which may rupture into smaller clusters by large enough applied stresses and then restores at a low stress level. The network needs time to build up and to disintegrate, and the rheology of the mixture therefore has a time scale; this results in a macroscopic thixotropic and yield stress behaviour, which has been considered one of the most complex phenomena in rheology [1]. For example, in cohesive sediment mixtures, which provide the motivation of this work, clay particles flocculate and then break up under flow conditions. At a low concentration some clay particles may form clusters and once the concentration reaches a threshold value, those clusters link up and form a network, leading to a yield stress behaviour.

In continuum mechanics, such yield-stress materials are modelled by a rel-

evant constitutive equation (the simplest model would be the Bingham model [3] or one of its variants). These models, representing a true solid-to-fluid transition behaviour without thixotropic complications, are transformed into sets of algebraic equations by means of discretisation and their flows are then solved numerically by traditional numerical methods, such as finite volume (FVM), finite element (FEM) or boundary element (BEM) methods. Because of the solid-to-fluid transition at small applied stresses, a "numerical singularity", associated with the indeterminate nature of the stress, occurs at low strain rates when dealing with these types of constitutive equations. To mitigate this numerical difficulty, Papanastasiou [4] proposed a modified version of Bingham model, which is in fact a generalised Newtonian model with high viscosity at low enough strain rate; thus replacing the transition to solid-like behaviour by a very viscous behaviour at low strain rates. Mathematically, Papanastasiou's model may be regarded as a regularisation of the Bingham model [5]. Papanastasiou's model has been widely used in many engineering applications [6]. However, it has been pointed out that, in practice, many substances, such as food products, crude oils, cohesive sediment mixtures display flow characteristics that may not be described by the Bingham models, or its viscous (regularised) approximations (we refer to these models as Bingham-type models). This is primarily because their apparent viscosities do not only depend on applied shear stresses, but also the duration for which the fluids have been subjected to the flow processes, as well as their previous kinematic history. Those fluids may be classified as thixotropic fluids. To describe the behaviour of thixotropic fluids, another approach which based on structural kinematics theory has been proposed (for instance, [1]; [7]; [8]; [9]). In these models, the time dependent rheological behaviour is quantified by a non-dimensional structural parameter λ. The scalar λ indicates the integrity of a particulate network, i.e., $\lambda = 0$: no network and $\lambda = \lambda_0$: a network is fully formed (λ_0 is the maximum value of λ, usually set to unity). The viscosity and the stresses are thus functionals of $\lambda(t)$; t is the time. Both the Bingham-type (now depend on $\lambda(t)$) and a relevant thixotropic model (for $\lambda(t)$) are simultaneously solved together with the Navier-Stokes equations to obtain

a specific solution, subjected to a relevant set of boundary/initial conditions.

In the last two decades the DPD method [10] has been developed as an alternative and promising mesoscopic approach for modelling complex fluids. Different from spatial macroscopic schemes, the DPD method is originally based on a coarse-grained representation of the fluid and everything in it. DPD method often looks similar to Molecular Dynamics (MD), with built-in thermal equilibrium via a fluctuation-dissipation theorem [11]. However, DPD particles interact through soft potentials and thus the simulation can be carried out on length and time scales far beyond those associated with MD. It has been shown that mean quantities (e.g., density and linear momentum) formed from the microstate of a DPD system (consisting of DPD particles positions and velocities) satisfy mass and momentum conservations [12]. Therefore, the method may be regarded as a particle-based method for solving complex fluid problems [13]. From this point of view, a single DPD particle may be regarded as similar to a smoothed particle hydrodynamics (SPH) particle (in its implementation), in which a certain volume of fluid is represented as a Lagrangian particle in the SPH method. Especially, in one of DPD variants called the smoothed DPD method (sDPD) [14], the interaction forces have a specific form which comprised from the SPH discretisation of Navier-Stokes equations. Many applications of DPD method or its variants in the simulations of complex fluids have been reported, e.g., sphere colloidal suspensions ([15]; [16]; [17]; [18]; [19]; [20]), colloidal suspensions of spheres, rods, and disks [21], viscoelastic fluid [22], ferromagnetic colloidal suspension [23], magnetic colloidal dispersions [24], soft matter and polymeric applications [25], [26], lipid bilayer [27], flows of DNA suspensions [28], polymer chains [29], red blood cell modelling [30], [31]; this list is not meant to be exhaustive.

The continuum approaches including Bingham-type models and/or structural kinetics models may be classified as top-down approach, which starts with the macro behaviour of the systems. In this paper, we report a DPD method, as a bottom-up approach, built on a microstructure interaction model, which yields the desired observed macro properties. An indirect linkage model for

dissipative particles through a micro interaction forces is proposed to mimic the formation of particulate network in a natural way. The continual forming, breaking and recovering of the microstructures results in yield stress together with the desired thixotropic behaviours.

The number density, fluid velocities and stresses in our DPD model are calculated by ensemble averaging the instant data (e.g., particle configuration, particle velocities, etc.), or by time-averaging over a number of time steps (with the assumption of the ergodic theorem). The stress-strain rate relation of the fluid is studied for Couette and Poiseuille flows. It is found that the numerical results can fit well to Papanastasiou's model at steady state. The DPD model also replicates thixotropic behaviour in a natural way, in unsteady flows, through the continual forming and rupturing of DPD microstructure network under applied stresses.

The remainder of the paper is organised in the following manner. An overview of the standard DPD fluid is provided in Section 2. Then, Section 3 gives a brief review of Bingham model, its variants and some prominent structural kinetics models. The proposed indirect linkage dissipative model is then presented in Section 4. Subsequently, in Section 5 and 6, a material preparing process is described, akin to an experimental process, and numerical results are discussed. Section 7 gives some concluding remarks.

2. Dissipative Particle Dynamics (DPD)

2.1. DPD fluid

DPD is a particle-based simulation method that satisfies mass and momentum conservations. It is a promising method, originally devised for simulations at mesoscopic length and time scale for material with a complex microstructure. The DPD method produces field results that satisfy the Navier-Stokes equations, in the same manner of other standard continuum methods (e.g., FEM, FVM, BEM), and therefore it can be regarded as a particle-based discretisation of the Navier-Stokes equations in mesoscale where thermal fluctuations are accounted

for. In DPD method, the fluid and all its component phases (if any) are defined by the assemblage of N particles, each of mass $m_i, i = \{1, 2, \ldots, N\}$ located at position $\mathbf{r}_i$, with velocity $\mathbf{v}_i$. With the assumption of identical mass, without much loss of generality, $m_i = m$, the DPD particles interact with each other and undergo their Langevin motions [32]:

$$\frac{d\mathbf{r}_i}{dt} = \mathbf{v}_i, \tag{1}$$

$$m\frac{d\mathbf{v}_i}{dt} = \mathbf{f}_i + \mathbf{f}_e, \tag{2}$$

where $\mathbf{f}_e$ is external forces on particle i (e.g., gravity force), $\mathbf{f}_i = \Sigma_{j\neq i}\mathbf{f}_{ij}$ ($\mathbf{f}_{ii} = 0$) the interaction force on particle i by all other particles j, pairwise additive. It is noted that the sum runs over all other particles within a certain cut-off radius r_c. The interaction force $\mathbf{f}_{ij}$ consists of three parts, a conservative force, $\mathbf{f}_{ij}^C$, a dissipative force, $\mathbf{f}_{ij}^D$, and a random force, $\mathbf{f}_{ij}^R$:

$$\mathbf{f}_{ij} = \mathbf{f}_{ij}^C + \mathbf{f}_{ij}^D + \mathbf{f}_{ij}^R. \tag{3}$$

Expressions of interaction forces are listed in Table 1 in which a_{ij} is conservative force strength; $\mathbf{r}_{ij} = \mathbf{r}_i - \mathbf{r}_j$; $r_{ij} = |\mathbf{r}_{ij}|$; $\widehat{\mathbf{r}}_{ij} = \mathbf{r}_{ij}/|\mathbf{r}_{ij}|$;w^C, w^D, w^R weight functions of conservative, dissipative and random forces, respectively; $\mathbf{v}_{ij} = \mathbf{v}_i - \mathbf{v}_j$; γ a coefficient related to the system viscosity; ξ_{ij} a Gaussian variable with zero mean and variance equal to δt^{-1}, where δt is the time step, and σ is the magnitude of the random force.

Table 1: List of interaction forces and their formulas. Note that the balance between dissipative and random forces must obey the fluctuation-dissipation theorems $\sigma = \sqrt{2\gamma k_B T}$ and $w^D = (w^R)^2$ [32].

$\mathbf{f}_{ij}$	Weight function	Form
$\mathbf{f}_{ij}^C$	$w^C(r_{ij}) = 1 - \frac{r_{ij}}{r_c}$	$a_{ij}w^c\widehat{\mathbf{r}}_{ij}$
$\mathbf{f}_{ij}^D$	$w^D(r_{ij}) = \left(1 - \frac{r_{ij}}{r_c}\right)^k$	$-\gamma w^D(\widehat{\mathbf{r}}_{ij} \cdot \mathbf{v}_{ij})\widehat{\mathbf{r}}_{ij}$
$\mathbf{f}_{ij}^R$	$w^R(r_{ij}) = \sqrt{\left(1 - \frac{r_{ij}}{r_c}\right)^k}$	$\sigma w^R\zeta_{ij}\widehat{\mathbf{r}}_{ij}$

2.2. Conservation properties

From the system state, one can define the local fluid density:

$$\rho\left(\mathbf{r},t\right)=\left\langle \sum_{i}m\delta\left(\mathbf{r}-\mathbf{r}_{i}\right)\right\rangle =md\left(\mathbf{r},t\right), \tag{4}$$

where the symbol $\langle\rangle$ indicates an ensemble average (which can be equated to a suitable time average over some iteration steps by the ergodic theorem), and $d\left(\mathbf{r},t\right)$ is the number density. The local linear momentum is calculated by

$$\rho\left(\mathbf{r},t\right)\mathbf{u}\left(\mathbf{r},t\right)=\left\langle \sum_{j}m\mathbf{v}_{j}\delta\left(\mathbf{r}-\mathbf{r}_{j}\right)\right\rangle . \tag{5}$$

These quantities have been shown to satisfy conservation laws ([12]; [32]):

$$\frac{\partial}{\partial t}\rho\left(\mathbf{r},t\right)+\nabla\cdot\left(\rho\left(\mathbf{r},t\right)\mathbf{u}\left(\mathbf{r},t\right)\right)=0,\qquad\nabla=\partial/\partial\mathbf{r}, \tag{6}$$

and

$$\frac{\partial}{\partial t}\left(\rho\mathbf{u}\right)+\nabla\cdot\left(\rho\mathbf{u}\mathbf{u}\right)=\nabla\cdot\boldsymbol{\sigma}. \tag{7}$$

Thus, DPD may be regarded as a particle-based method for solving continuum flow problems Eqs.(6)-(7). The macroscopic properties including fluid density ρ, stress $\boldsymbol{\sigma}$ and consequentially viscosity μ are calculated by appropriate averages over all sampled data in each bin. The relevant stress tensor $\boldsymbol{\sigma}$ is calculated by Irving-Kirkwood expression ([33]). In one dimensional shear flow, the fluid viscosity can be found from the shear stress and the shear rate, $\mu=S_{xz}/\dot{\gamma}$. In this particle-based point of view, a DPD particle may be thought of as a volume of fluid with a built-in behaviour (e.g., a non-Newtonian viscous compressible fluid volume), rather than a cluster of fluid molecules. Yield stress and thixotropic behaviours may also be captured by this particle-based method. The nonlinear relationship between stress and strain rate needs not to be specified a-priori, but can be obtained after post-processing step.

3. Brief review of yield stress fluid models

3.1. Bingham models

In continuum mechanics, Bingham plastic is a non-Newtonian fluid behaviour characterised by the existence of a threshold stress called the apparent yield stress (S_0), which must be exceeded for the fluid to deform (shear) or flow. Such behaviour can be modelled by a simple Bingham rheological constitutive model ([3], [5]):

$$\mathbf{S} = 2\left\{\mu + \frac{S_0}{\mathbb{III}_D^{1/2}}\right\}\mathbf{D}, \qquad |\mathbf{S}| > S_0. \tag{8}$$

In the above, $\mathbf{S}$ is the extra stress; $\mathbb{III}_D^{1/2}$ denoted the generalised strain rate; $\mathbb{III}_D$ the second invariant of strain rate tensor $\mathbf{D}$,

$$\mathbf{D} = \frac{1}{2}\left(\nabla\mathbf{u} + \nabla\mathbf{u}^T\right), \tag{9}$$

where $\nabla\mathbf{u}^T$ the velocity gradient tensor (by definition). $|\mathbf{S}|$ the magnitude of the extra stress tensor and is defined as

$$|\mathbf{S}| = \sqrt{\frac{1}{2}\left[\mathbf{S} : \mathbf{S}\right]}. \tag{10}$$

Below the stress threshold, the stress is inderterminate, and while this is an engineering simplification, this discontinuity in behaviour is a major problem in numerical implementation. Papanastasiou [4] proposed a modified version of Bingham model to overcome this numerical difficulty by introducing an exponential regularisation for the stress and strain rate relation in Eq.(8); more details of this regularisation can be found in [5]. Here the stress is written as

$$\mathbf{S} = 2\left\{\mu + \frac{S_0\left[1 - e^{\left(-n\mathbb{III}_D^{1/2}\right)}\right]}{\mathbb{III}_D^{1/2}}\right\}\mathbf{D}, \tag{11}$$

where n is a stress growth parameter which determines how fast the development of stress. It is noted that n does not have physics meaning, although it has the dimension of time, and it is set to a large enough value that does not cause numerical instability. In one dimensional problems, $\mathbb{II}_D^{1/2}$ becomes the shear rate $\dot{\gamma}$. At high shear rate where the second term in the curly brackets approaches zero, this model asymptotes to $2\mu\mathbf{D}$, a Newtonian fluid with viscosity μ. At low strain rate, the stress asymptotes to $2(\mu + nS_0)\mathbf{D}$. Consequently, for large n, this fluid model is close to Bingham model, in the sense that the deformation at low strain rate is small because of the large viscosity, but the true solid-to-fluid transition (as embodied in the Bingham model) is lost, and is now replaced by a very viscous transition.

3.2. Structural kinetics model

Qualitative concept of particulate networks

A well-dispersed system, such as a dense cohesive sediment suspension, displays rheological characteristics which cannot be simply described by mathematical expression of the form of Eqs.(8) or (11). In fact their viscosity and yield stress are not only functions of the applied shear rate ($\dot{\gamma}$), but also their previous shear history.

Similar to Bingham-type fluids, this type of non-Newtonian fluids exhibit a yield stress S_0: it will flow in a whole like a solid body when externally applied stresses are less than S_0. Naturally, when the magnitude of the external stress exceeds S_0, the fluid may exhibit shear-thinning effect. Such a fluid at rest consists of small attractive particles which form a cluster to produce a structure network of sufficient connectivity - this structure can resist any applied stress less than S_0 without deformation. In contrast, if the applied stress magnitude is greater than S_0, the structure network breaks down and thus results in a decreasing resistance to deformation and flow. The reversed may also happen, i.e., the fluid may restore some of its network connectivity, and the yield stress value of the recovered state may be equal or lower than that of the initial state.

Thixotropy model

To quantify the structure dependent rheological behaviour, a non-dimensional structural parameter λ has been used to characterise any fluid parameter, for example viscosity or yield stress may be expressed as functionals of this parameter, i.e., $\mu(\lambda(t))$, or $S_0(\lambda(t))$ [9]. This parameter is a measurement of the degree of structure in the dispersed system, having a value in the range 0 (fully broken) to λ_0 (fully structured), commonly assumed to be unity. In a one-dimensional problem, a simple model of λ's evolution may be described by a first-order rate equation:

$$\frac{d\lambda}{dt} = \frac{\partial \lambda}{\partial t} + u_x \frac{\partial \lambda}{\partial x} = a(\lambda_0 - \lambda) - b\dot{\gamma}\lambda, \tag{12}$$

where u_x the $x-$component of the fluid velocity vector (the only relevant component in this 1D problem); a and b two coefficients determined from experiments. The first term on the right side of (12) represents the network coalescence with the associated constant a; and in the second term, the constant b represents the disintegration of the particulate network due to the flows. The equilibrium value of the structural parameter λ_e can be obtained by equating the right side of (12) to zero:

$$\lambda_e = \frac{a\lambda_0}{a + b\dot{\gamma}} = \frac{\lambda_0}{1 + \beta\dot{\gamma}}, \tag{13}$$

where $\beta = b/a$.

A rheological equation for a thixotropic yield stress fluid has been proposed by [9] (in 1D)

$$S_{xz} = (\lambda_0 + \lambda - \lambda_e)S_0 + (\mu_\infty + c\lambda)\dot{\gamma}. \tag{14}$$

At equilibrium, when the rate of disintegration equals the rate of recovery, the equilibrium flow (EF) curve is characterised by evaluating Eq.(14) at equilibrium point $\lambda = \lambda_e$ and using the relation (13) :

$$S^e_{xz} = \lambda_0 S_0 + \mu_\infty \dot{\gamma} + \frac{c\lambda_0\dot{\gamma}}{1 + \beta\dot{\gamma}}. \tag{15}$$

Thixotropic fluids may exhibit a family of stress/strain rate curves called constant structure (CS) curves [34], each one corresponding to a (constant) value

of its structure parameter. The EF curve and CS curves intersect at points on which the structure is equilibrium (Figure 1). Consider a CS curve which cut across the EF curve at equilibrium point E. At points above the EF curve (e.g., point A), if the shear rate is kept constant, the structure will break resulting in a reduction in the shear stress S^A to equilibrium value S_e^A. In contrast, at points below the EF curve, such as point B, the structure will continually build up and the shear stress S^B would raise until the system reaches the equilibrium state ($S = S_e^B$). When the EF curve is known and can be described by Eq.(15), a simple procedure allows the determination of the CS curves (either numerically or experimentally). For example, consider an ith data point of the EF curve, one has a CS curve which have a single value of structural parameter λ_i. The value of λ_i is the same of λ_E at the crossover point of this CS and the EF curves. Substitution of this value into Eq.14 gives the CS curve of the ith point,

$$S = (\lambda_E + \lambda_e \beta \dot{\gamma}) S_0 + (\mu_\infty + c\lambda_E)\dot{\gamma}. \tag{16}$$

4. Proposed indirect linkage dissipative particle (ILDP) model

Inspired from this qualitative concept of a particulate network, we propose the following DPD model consisting of *two types DPD particles*, represented by the ensemble of $N = N^{(a)} + N^{(b)}$ particles, each of the set of $N^{(s)}$ particles represents number of particles in each species $s = a$ or b of the fluid. Among $DPD^{(a)}$ and $DPD^{(b)}$ particles, there are three types of interactions: $DPD^{(a)}$ to $DPD^{(a)}$ or (a,a), $DPD^{(b)}$ to $DPD^{(b)}$ or (b,b), and $DPD^{(a)}$ to $DPD^{(b)}$ or (a,b). Here $\mathbf{f}_{ij}^{(a,b)}$ is the pairwise additive interparticle force by particle $j(b) \in N^{(b)}$ on particle $i(a) \in N^{(a)}$ (the notation $i(a)$ reads particle i in species a). To avoid a phase separation between (a) and (b), we propose an indirect linkage by introducing cohesive forces between $DPD^{(a)}$ and $DPD^{(b)}$ particles. The indirect linkage dissipative particle model (ILDP) thus comprises from (a, a) or (b, b) interactions with repulsive force (the "standard" model for DPD fluid), and long-range attractive plus short-range repulsive ((a, b) or (b, a)) - the network of

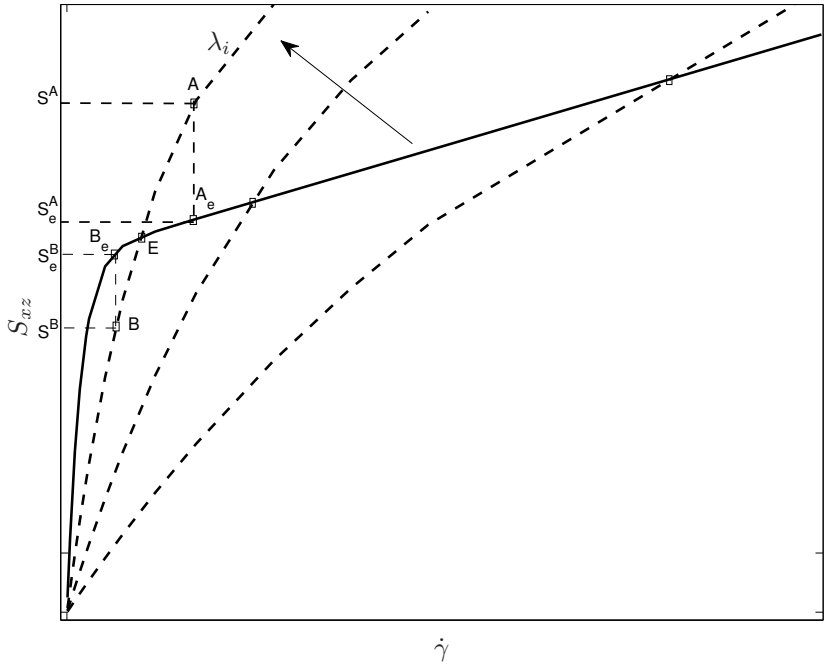

Figure 1: Equilibrium flow curve (solid line) and constant structure curves (dash lines). The arrow indicates that the structural levels increase (not to scale).

$DPD^{(b)}$ can be encouraged to form by adding a long-range attractive component to the conservative forces, which is taken from [35]. It is important to note that $DPD^{(b)}$ particles attract $DPD^{(a)}$ directly, and $DPD^{(b)}$ indirectly. $DPD^{(b)}$ particles form an indirect network though layers of $DPD^{(a)}$ particles (Figure 2). In this model, we view $DPD^{(a)}$ and $DPD^{(b)}$ as a solvent and suspended phase, respectively.

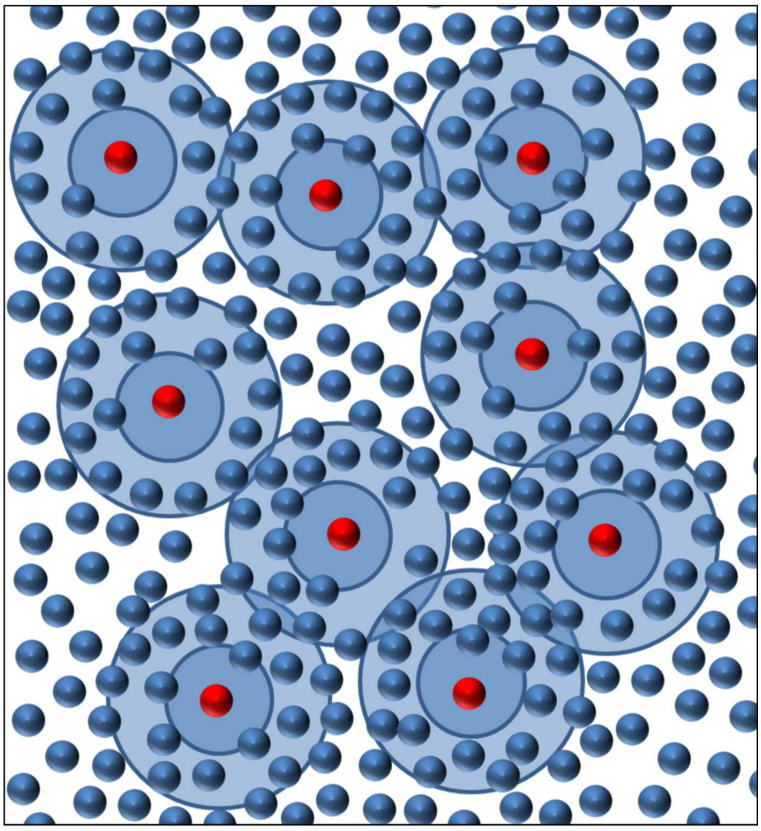

Figure 2: Indirect linkage DPD network: Microstructure of the proposed model-two species of DPD ($DPD^{(a)}$ (blue colour)) and $DPD^{(b)}$ (red colour)). A $DPD^{(b)}$ attracts some $DPD^{(a)}$ within its long range (circles of larger radius) and repulses other $DPD^{(b)}$ and $DPD^{(a)}$ in short range (circles of smaller radius).

Assuming that each DPD particle of a species s has a mass of $m_i^{(s)}$ located at position $\mathbf{r}_i^{(s)}$, with velocity $\mathbf{v}_i^{(s)}$. The DPD particles interact with each other in their Newton's second law motions:

$DPD^{(a)}$:

$$\frac{d\mathbf{r}_i^{(a)}}{dt} = \mathbf{v}_i^{(a)}, \quad m_i^{(a)} \frac{d\mathbf{v}_i^{(a)}}{dt} = \sum_{j \neq i} \mathbf{f}_{ij}^{(a,b)} + \sum_{j \neq i} \mathbf{f}_{ij}^{(a,a)}. \tag{17}$$

$DPD^{(b)}$:

$$\frac{d\mathbf{r}_i^{(b)}}{dt} = \mathbf{v}_i^{(b)}, \quad m_i^{(b)} \frac{d\mathbf{v}_i^{(b)}}{dt} = \sum_{j \neq i} \mathbf{f}_{ij}^{(b,a)} + \sum_{j \neq i} \mathbf{f}_{ij}^{(b,b)}. \tag{18}$$

Similar to the conventional DPD, $\mathbf{f}_{ij}$ consists of three parts, a conservative force $\mathbf{f}_{ij}^C$, a dissipative force $\mathbf{f}_{ij}^D$, and a random force $\mathbf{f}_{ij}^R$. In Eqs.(17)-(18), the sum runs over all other particles except i (note, by definition $\mathbf{f}_{ii}^{(s,s)} = \mathbf{0}$). These forces are built-in with a certain cut-off radius r_c; outside this cut-off radius, the interactions are zero. Here one may allow the cut-off radius to be different for different type of forces. The dissipative and random forces are taken the same forms listed in Table 1. Conservative force $\mathbf{f}_{ij}^C$ of $DPD^{(a)}$ and $DPD^{(b)}$ interaction is calculated according to the model proposed by [35]

$$\mathbf{f}_{ij}^C = -a_{ij}(Aw^{Cr}(r, r_r) - Bw^{Ca}(r, r_a))\widehat{\mathbf{r}}_{ij}, \tag{19}$$

where A and B are coefficient of $w^{Cr}(r, r_r)$ and $w^{Ca}(r, r_a)$, respectively. r_r is cut-off radius of repulsive component and r_a is that of attractive component and

$$w^{Cr} = \begin{cases} 18\left(\frac{A}{r_r^3} - \frac{B}{r_a^3}\right) r^2 - 12\left(\frac{A}{r_r^2} - \frac{B}{r_a^2}\right) r, r < \frac{r_r}{2} & (a) \\ -6\left(\frac{A}{r_r^3} + \frac{B}{r_a^3}\right) r^2 + 12\left(\frac{A}{r_r^2} + \frac{B}{r_a^2}\right) r - 6\frac{A}{r_r}, \frac{r_r}{2} \leq r < \frac{r_a}{2} & (b) \\ -6\left(\frac{A}{r_r^3} - \frac{B}{r_a^3}\right) r^2 + 12\left(\frac{A}{r_r^2} - \frac{B}{r_a^2}\right) r - 6\left(\frac{A}{r_r} - \frac{B}{r_a}\right), \frac{r_a}{2} \leq r < r_0 & (c) \\ 0, r > r_0 & (d) \end{cases} \tag{20}$$

$$w^{Ca} = \begin{cases} 0, r < r_0 & (a) \\ -6\left(\frac{A}{r_r^3} - \frac{B}{r_a^3}\right) r^2 + 12\left(\frac{A}{r_r^2} - \frac{B}{r_a^2}\right) r - 6\left(\frac{A}{r_r} - \frac{B}{r_a}\right), r_0 \leq r < r_r & (b) \\ 6\frac{B}{r_a^3} r^2 - 12\frac{B}{r_a^2} r + 6\frac{B}{r_a}, r_r \leq r < r_a & (c) \end{cases} \tag{21}$$

where value of r_0 is the solution of quadratic equation (20(c)).

The conservative, dissipative and random forces are taken as follows

$$\mathbf{f}_{ij}^{C(a,a)} = \mathbf{f}_{ij}^{C(b,b)} = \mathbf{f}_{ij}^{Cr}, \tag{22}$$

$$\mathbf{f}_{ij}^{C(a,b)} = \mathbf{f}_{ij}^{C(b,a)} = \mathbf{f}_{ij}^{Cr} + \mathbf{f}_{ij}^{Ca}, \tag{23}$$

$$\mathbf{f}_{ij}^{D(a,a)} = \mathbf{f}_{ij}^{D(b,b)} = \mathbf{f}_{ij}^{D(a,b)} = \mathbf{f}_{ij}^{D}, \tag{24}$$

$$\mathbf{f}_{ij}^{R(a,a)} = \mathbf{f}_{ij}^{R(b,b)} = \mathbf{f}_{ij}^{R(a,b)} = \mathbf{f}_{ij}^{R}. \tag{25}$$

With the same mass, i.e., $m_i^{(a)} = m_i^{(b)} = m$, Eqs.(17)-(18) can be rewritten as

$$m\frac{d\mathbf{v}_i}{dt} = \begin{cases} \sum\limits_{j\neq i} \left(\mathbf{f}_{ij}^{Cr} + \mathbf{f}_{ij}^{D} + \mathbf{f}_{ij}^{R}\right), & i,j \in N^{(a)} \quad or \quad i,j \in N^{(b)} \quad (a) \\ \sum\limits_{j\neq i} \left(\mathbf{f}_{ij}^{Cr} + \mathbf{f}_{ij}^{Ca} + \mathbf{f}_{ij}^{D} + \mathbf{f}_{ij}^{R}\right), & i \in N^{(a)}, j \in N^{(b)} \quad or \quad i \in N^{(b)}, j \in N^{(a)} \quad (b) \end{cases} \tag{26}$$

where $\mathbf{f}_{ij}^{Ca} = a_{ij} B w^{Ca} \widehat{\mathbf{r}}_{ij}$ and $\mathbf{f}_{ij}^{Cr} = -a_{ij} A w^{Cr} \widehat{\mathbf{r}}_{ij}$.

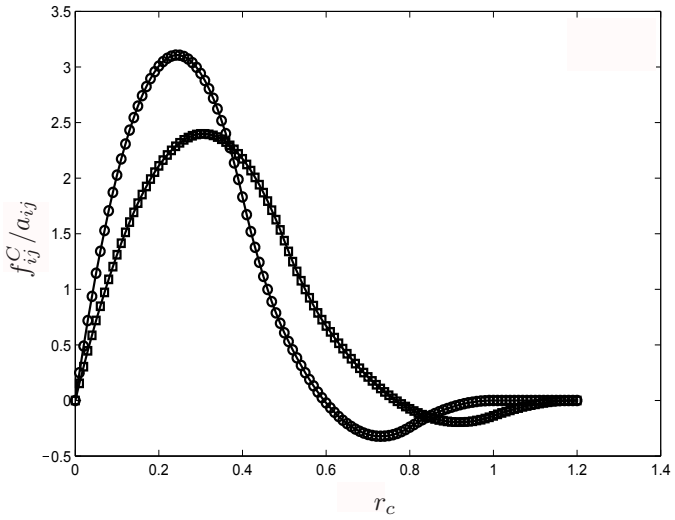

Figure 3: Conservative forces with short range repulsion and long range attraction ($-\circ$, $r_a = 1.0$) and ($-\square$, $r_a = 1.2$).

It can be seen from Figure 3 that the conservative force between two different

species particles is repulsive when their separation distance is less than a radius value of r_0, e.g., 0.5952, for $A = 2, B = 1, r_r = 1.0, r_a = 1.2$; and when their separation distance is between 0.5952 and 1, this force describes a long range attraction (negative). If purely repulsive conservative forces (for example, when setting $B = 0$ in Eq.(19), for $DPD^{(b)}$), are applied for both type particles, the resulting DPD fluid is thus simply Newtonian. When the attractive component in conservative forces of $DPD^{(b)}$ are turned on, a structure network is formed resulting in high DPD fluid's resistance to applied stresses. The advantages of indirectly linking between $DPD^{(b)}$ include (i) simple and straight forward to implement, (ii) uniform distribution for $DPD^{(a)}$ and $DPD^{(b)}$ (without phase separation), and (iii) creating a DPD structure network which results in yield stress and thixotropic behaviour. In next sections, numerical experiments are carried out for this proposed model.

5. Material preparation

5.1. Pre-processing

A pre-processing program is used to generate a system which consists of N particles with masses m characterised by the positions $\mathbf{x}_i, i = 1, N$. There are three types of particles in this list: wall, $DPD^{(a)}$ and $DPD^{(b)}$ particles. Initially (Figure 4a), the box is filled with $DPD^{(b)}$ particles in the bottom and with $DPD^{(a)}$ on the top. This initial distribution of these particles does not satisfy the thermodynamic equilibrium state, and a mixing procedure is thus applied. At the beginning of this procedure, the particles are allowed to move freely until a thermodynamic equilibrium state is reached and then a body force $\mathbf{g} = (0.2, 0, 0)$ is applied for a hundred thousand time steps to mix $DPD^{(a)}$ and $DPD^{(b)}$. Figure 4b shows that after mixing, the conservative interactions produced a uniform $DPD^{(a)}$ and $DPD^{(b)}$ dispersion. The particle configuration is written in a data file which is then read by the DPD solver program.

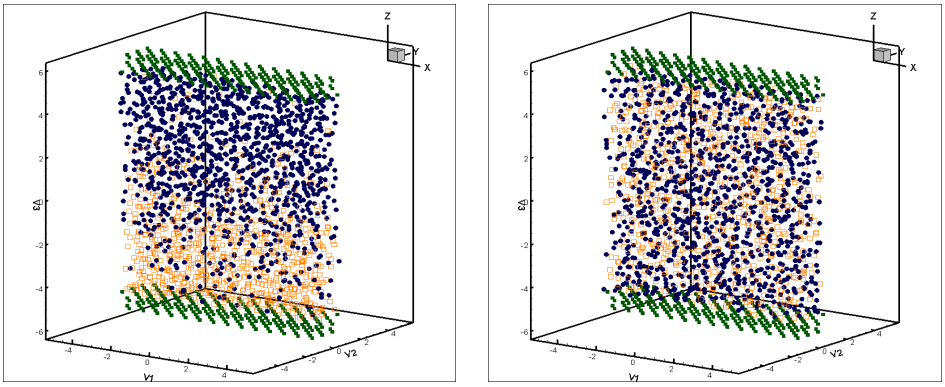

(a) (b)

Figure 4: A thick slide along the center line ($-0.5 \leq y \leq 0.5$): (a) Initial configuration of $DPD^{(a)}$ (•) and $DPD^{(b)}$ (□) - (b) Uniform distribution of two species of DPD, which are obtained over the period of 100000 time steps.

5.2. ILDP micro-networks

5.2.1. No flow

Before testing, all mixtures are set to a test kinetic energy $k_BT = 1$ and then let it run in no-flow condition for 40000 time steps, each of 0.01, to guarantee that the microstructure network is fully built up. To track the formation of the network, one may choose an ith particle of $b-$species and plot its position $|r| = \sqrt{x^2(i) + y^2(i) + z^2(i)}$. In this test, the dispersed system is allowed to reach equilibrium and the coefficient of attractive forces $\mathbf{f}^{Ca}$ are set to zero for the first 10000 time steps. It is then turned on to activate any particulate network. The value of $|r|$ and the trajectory of ith particle are plotted in Figure 5a and 5b, respectively. It is observed that the fluctuation of ith particles is reduced dramatically when the particulate network starts to form and the ith particle is trapped in a cage formed by its neighbouring particles, as expected.

5.2.2. Shear flow testing

In this section, the dependence of structure to the applied shear rate is investigated. The applied shear rate is a step function, for a time interval of 8000 time steps, each of 0.01. Initially, the DPD system is allowed to reach

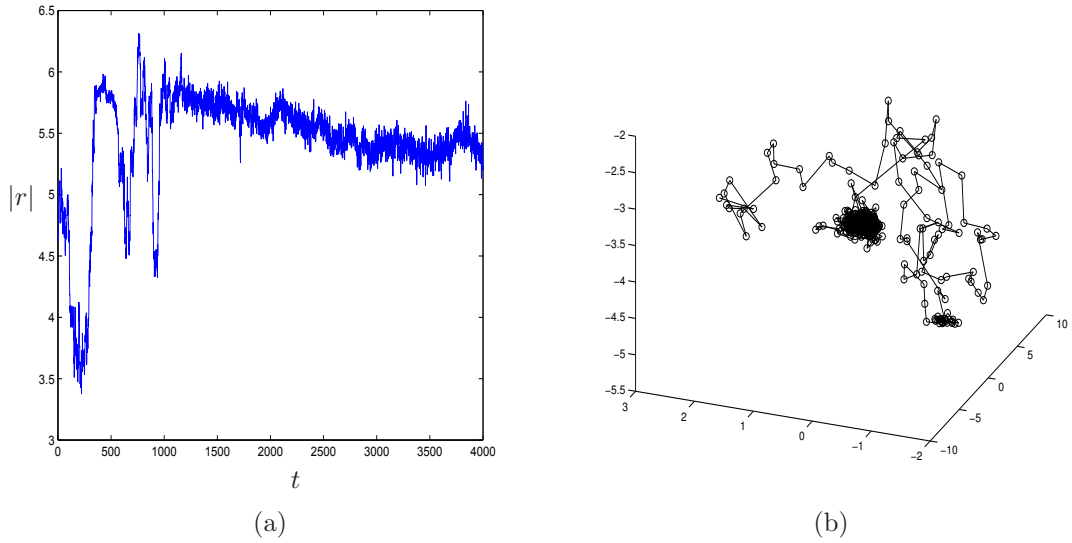

Figure 5: Structure forming: (a) The position $|r|$ and (b) the trajectory of an ith $DPD^{(b)}$ species particle, before and after the microstructure network built up.

equilibrium, the structure network is formed as displayed in Figure 6(a). Then, a shear rate $\dot{\gamma} = 1.0$ is applied; Figure 6(b) shows that the structure is totally destroyed. In a general flow, the level of integrity of the structure network depends on the local shear rate. After around 8000 time steps, the shear rate is returned to zeros, and it is observed that the structure network is restored (Figure 6(c)). Here, in order to have clearer configuration of the microstructure for visualisation purpose a relative large cut-off radius for attractive forces is employed ($r_a = 1.33$).

6. Numerical experiments and discussion

The ILDP fluid are tested in Couette and Poiseuille flows. The simulations are carried out on two domains, of $10 \times 10 \times 10$ and $20 \times 10 \times 20$ for Couette flow, and $10 \times 10 \times 10$ for Poiseuille flow; the DPD parameters are listed in Table 2.

For the conservative interaction of $DPD^{(a)}$ and $DPD^{(b)}$, we fix the repulsive and attractive coefficients at $A = 2$ and $B = 1$, respectively (Figure 3). For

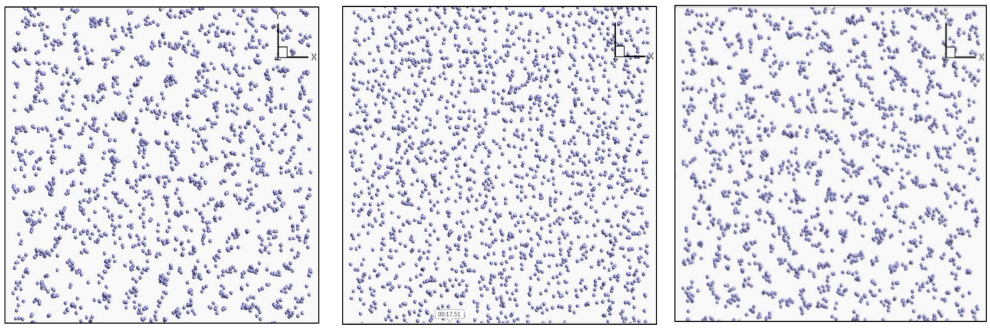

(a) (b) (c)

Figure 6: A snapshot of structure forming at initial state (a), and its breaking under an applied shear rate $\dot{\gamma} = 1$ (b), and then its reforming when the shear rate is reset to zero again (c). It is note that only $DPD^{(b)}$ particles are plotted.

the dissipative force listed in Table 1 $\mathbf{f}_{ij}^{D}$, in a modified version of DPD [28], two parameters are set as $1.0 \leq r_r \leq 1.5$ and $k = 1/2$, to enhance the dynamic response. We use the same setting $k = 1/2$, and fix the cut-off radius value r_r at 1.0 for both $DPD^{(a)}$ and $DPD^{(b)}$. The concentration ratio, ϕ, represents the amount of $DPD^{(b)}$ to the total mixture,

$$\phi = \frac{N^{(b)}}{N^{(a)} + N^{(b)}}. \tag{27}$$

The simulation is run with 140,000 time steps in which 40,000 time steps is used to ensure the system reaches a fully built-up structure, and after some experiments, a time step 10^{-2} is chosen for all simulations. Periodic boundary conditions are applied in $x-$ and $y-$direction, i.e., particles that pass one periodic face reappear in the domain at the opposite face, and therefore effectively an infinitely large, but periodic DPD system is being considered. In $z-$direction, solid walls are represented by three layers of frozen particles. It is known that conventional solid boundary models for DPD lead to slip at the boundary even at moderate applied shear rate. To reduce this, a wall wetting model [36] is employed in the Couette and Poiseuille flows to mimic a hydrophilic behaviour. Figure 7 shows that the non-slip boundary condition is improved with the latter

wall model. In all the following simulations, the Verlet integration algorithm is employed to solve Eq.(26).

Table 2: A typical DPD parameters.

a_{ij}	σ_{ij}	γ_{ij}	k_BT	m	d	A	B
18.75	3.0	4.5	1.0	1.0	9.8	2	1

In a manner similar to a physical experiment, here one can measure the yield stress S_0 by plotting the shear stress/shear rate curve, and then extrapolate the shear stress (on the Newtonian portion) onto the stress axis. This value on the stress axis gives us an approximation to the yield stress (Figure 8).

It is noted that the effective shear rate is calculated by ignoring the first and the last bin next to the top and bottom wall/boundaries particles. The shear rate used for plotting the shear stress/shear rate curve is thus the actual applied shear rate instead of the input shear rate. From the stress values calculated by post-processing, an average shear stress S_{xz} is computed and plotted against the actual shear rate, producing the flow curve at equilibrium for a specific set of parameters. It is useful here to use a continuum model, e.g., the Papanastasiou model for correlation. The curve fitting process using the optimisation Generalised Reduced Gradient algorithm (GRG) is carried out to fit DPD data into the continuum model.

6.1. Equilibrium flow curves

The range of input shear rates is $\dot{\gamma} = \{0.01, 0.02, 0.03, 0.05, 0.07, 0.09, 0.10, 0.15, 0.20, 0.30, 0.40, 0.60, 0.80, 1.0\}$, with a smaller interval at low shear rate for a better observation of the fluid behaviour at low shear rate. Here we let the system reaches equilibrium and then apply a constants shear rate (Figure 9). In this test it is noted that the steady state property of the fluid is of importance here.

An ILDP fluid with DPD parameters listed in Table 2, $\phi = 0.2$, and a cut-off radius $r_a = 1.3$ is selected for this measurement. The viscosity as a function of

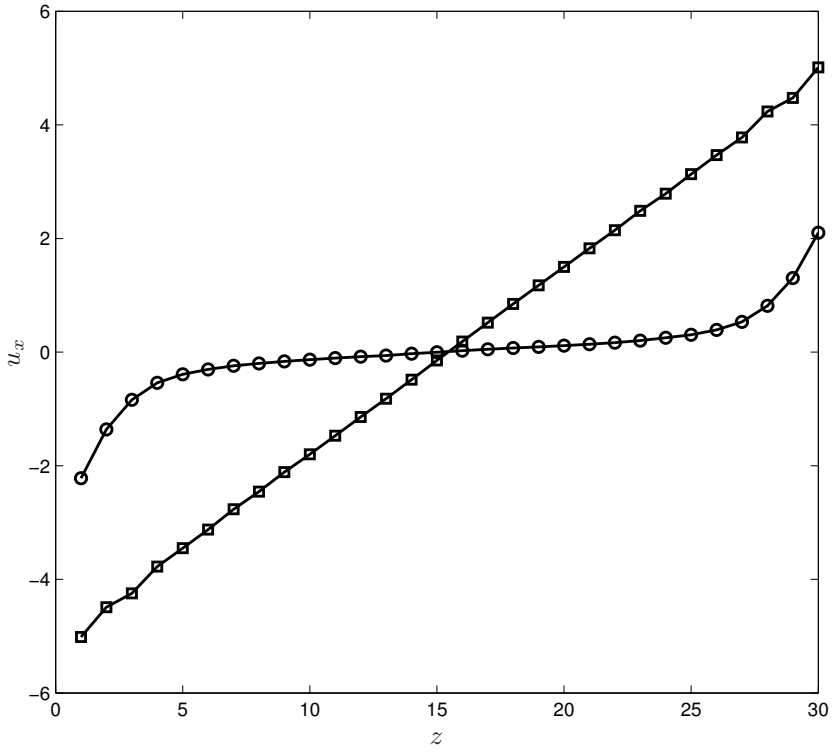

Figure 7: Velocity profile of Couette flow of an ILDP fluid (domain size $10 \times 10 \times 10$, $\dot{\gamma} = 1$) with two wall models: conventional solid boundary models ($-\circ$) and wall wetting model ($-\square$).

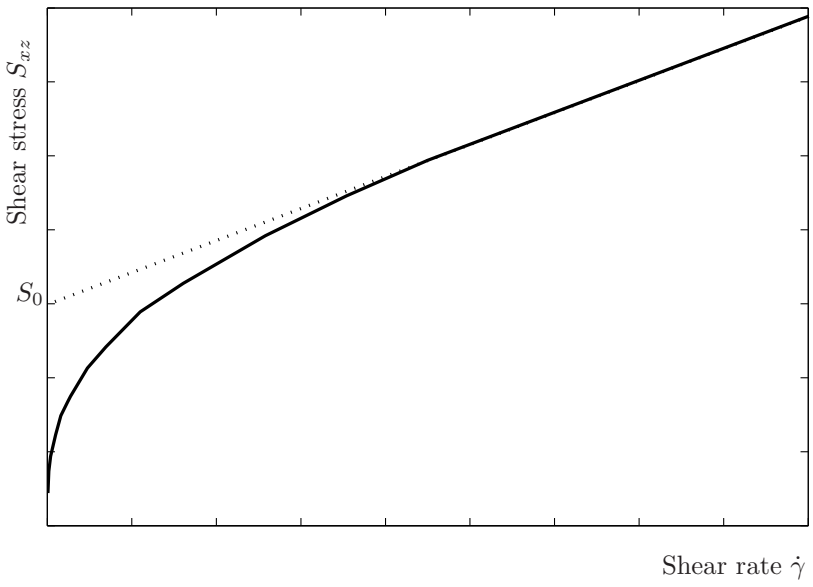

Figure 8: A typical nonlinear curve of shear stress versus shear rate. (Not to scale)

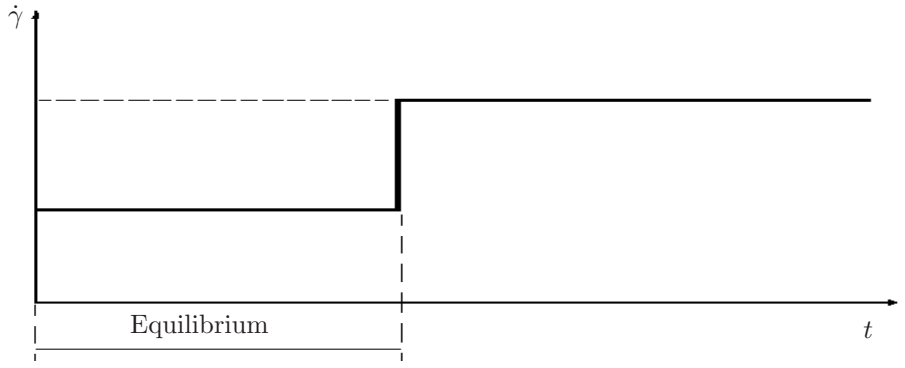

Figure 9: Couette flows: A typical applied shear rate. It is noted that the DPD system is allowed to reach equilibrium and the structures are fully built up after 40000 time steps.

shear rate is plotted in Figure 10. It is known that the flow breaks down the structure network into smaller clusters which results in reducing the apparent viscosity and thus shear-thinning behaviour appears. Numerical data show that viscosity decreases dramatically from 600 at applied shear rate 0.03 to 18.8 at applied shear rate 2.0. The Couette velocity profile, temperature and density fluctuation are presented in Figure 11. It can be seen that linear profile of velocity is obtained, and uniform distribution of density and temperature at the chosen time step $dt = 0.01$.

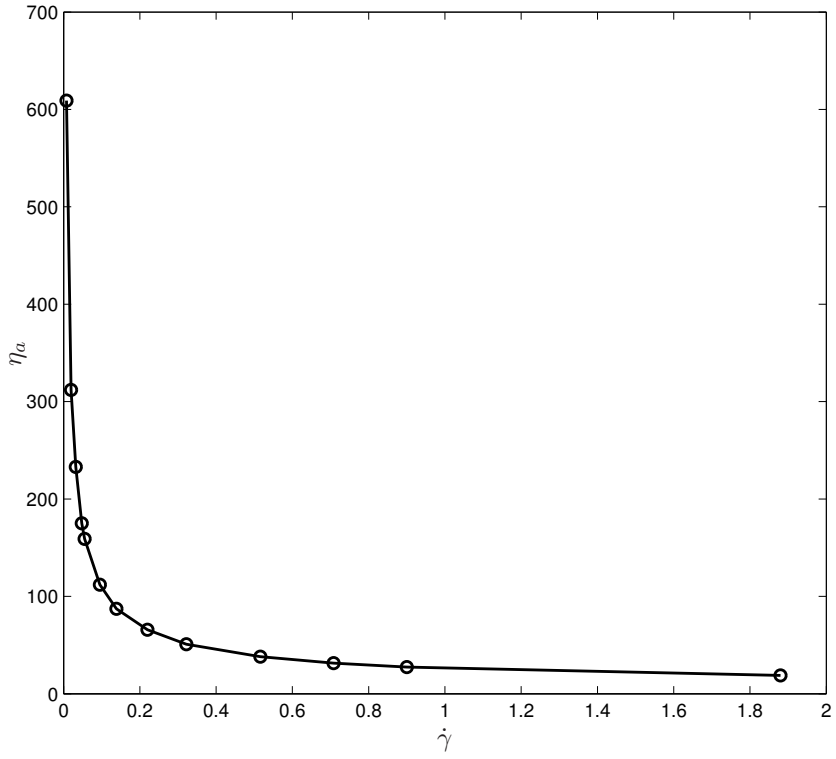

Figure 10: Couette flows (domain size $20\times10\times20$): apparent viscosity η_a plotted as a function of shear rate.

We give an example of using the flow curve of an ILDP fluid to model a foodstuff product, in this case a salad dressing. The steady shear data for

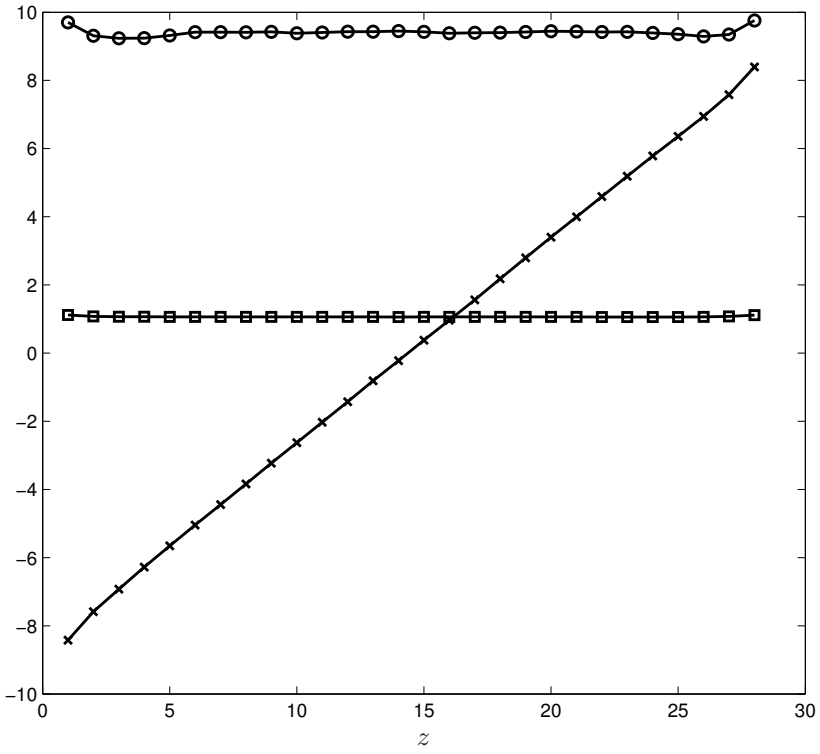

Figure 11: Couette flow (domain size $20 \times 10 \times 20$, $\dot{\gamma} = 0.5$): Profiles of velocity u_x ($-\times$), temperature $k_B T$ ($-\square$) and number density d ($-\circ$).

this salad dressing has been obtained at temperature 295K using a concentric cylinder viscometer ($R_1 = 20.04$ mm; $R_2 = 73$ mm; $h = 60$ mm) [37]. Table 3 shows salad dressing data with shear stresses and the shear rates normalised to $S_0 = 10.1Pa, \dot{\gamma}_0 = 11.396s^{-1}$, respectively. The DPD data has been collected by the same procedure with the example above with the set of DPD parameters listed in Table 2, $\phi = 0.2$. The degree of fit between experiment and numerical data is good, as shown in Figure 12.

Table 3: Couette flow: salad dressing data (dimensionless data).

$\dot{\gamma}/\dot{\gamma}_0$	S_{xz}/S_0
0.07	0.40
0.24	0.66
0.49	0.83
1.00	1.07
1.99	1.34
3.00	1.61
4.00	1.79
5.02	1.96
6.03	2.08
7.03	2.20
8.03	2.32

Numerical tests are performed on an ILDP fluid of varying kinetic energy $k_BT = \{0.7, 0.8, 0.9, 1.1, 1.2, 1.3, 1.4, 1.5, 2.0\}$. Smaller value of k_BT reduces the fluctuations in the systems. Non-linear shear stress/shear rate curves are plotted in Figure 13, at different k_BT. Clearly, the whole family of curves shifts up (i.e., increasing the parameter n in Papanastasiou's model) with decreasing the kinetic energy k_BT. It is observed that below the value k_BT of 0.7, numerical results show that the fluid is not flowing.

We also match the DPD behaviour with the Papanastasiou's model (11). Figure 14 shows the comparison. It can be seen that the data obtained by the DPD model can be fitted well to Papanastasiou's model - the GRG agorithm provides a viscosity of 12.21, stress growth parameter $n = 20$, and a yield stress of $S_0 = 9.98$.

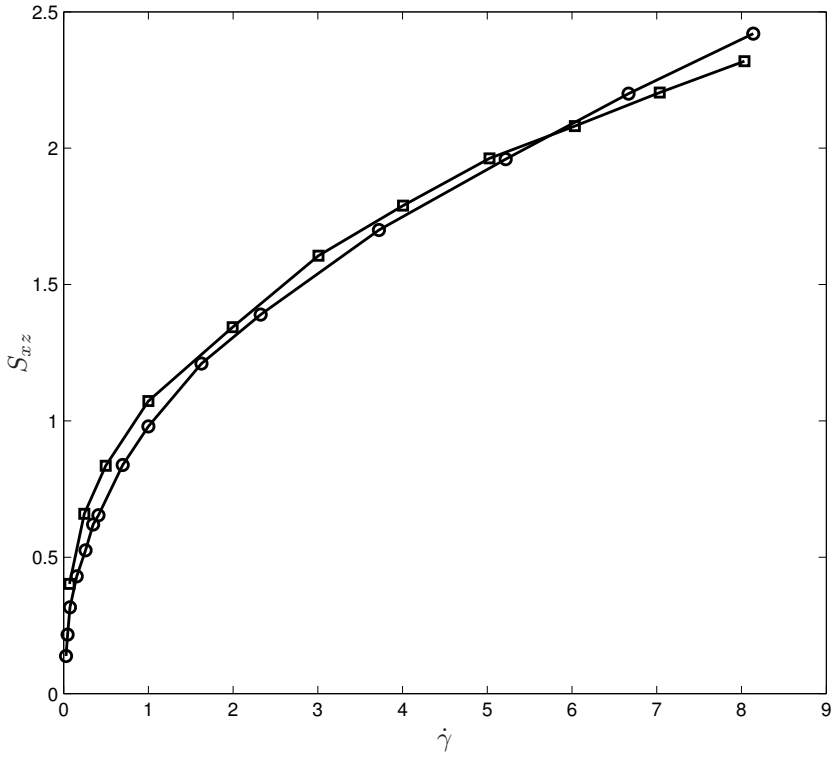

Figure 12: Couette flow: Shear stress/shear rate data for salad dressing data; −□ experiment, −○ DPD results.

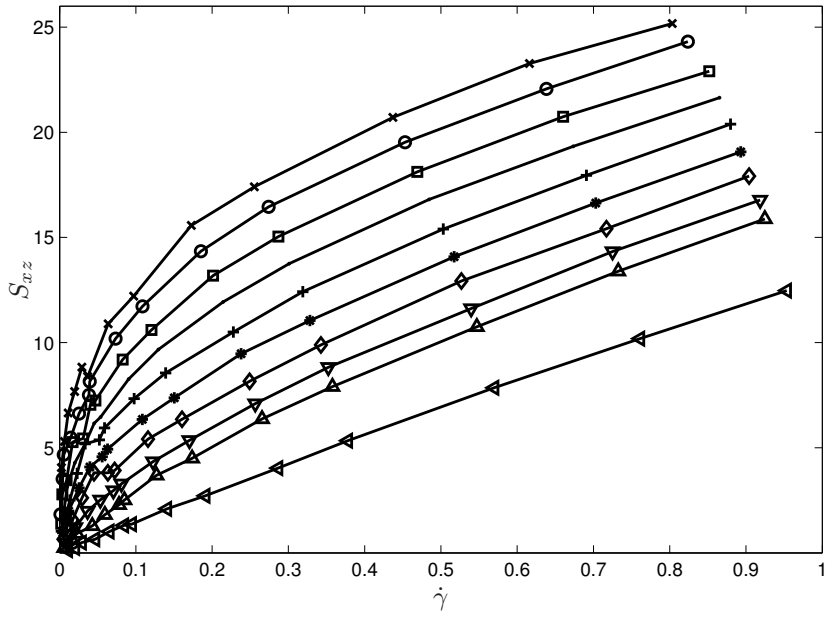

Figure 13: Couette flow: Non-linear shear stress - shear rate behaviour at different values of $k_BT = \{0.7, 0.8, 0.9, 1.0, 1.1, 1.2, 1.3, 1.4, 1.5, 2.0\}$, from top to bottom.

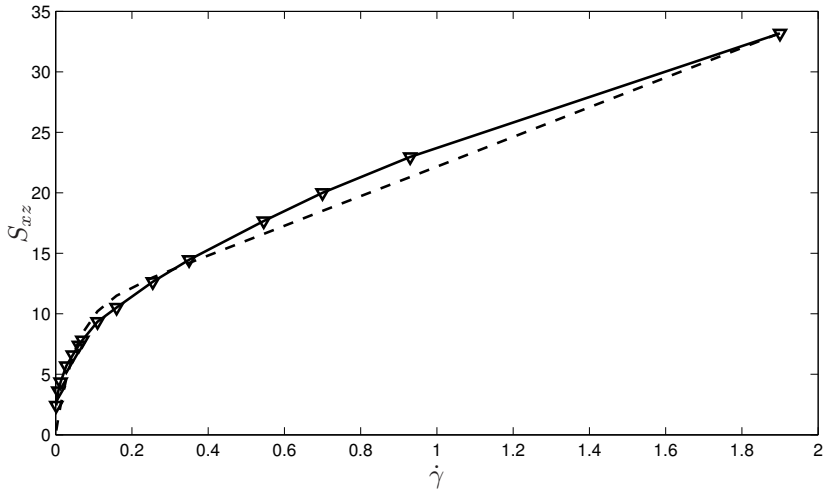

Figure 14: Couette flows: DPD data (Table 2, $\phi = 0.2, r_a = 1.3$)-solid line-can be fitted well to Papanastasiou's model-dash line-(Eq.11), with a low-shear viscosity of $\eta + nS_0 = 211.81$ (slope of the rheogram when shear rate smaller than 0.1) and a high-shear viscosity of $\eta = 12.21$ (slope of the rheogram when shear rate larger than 0.1)(all dimensionless).

6.1.1. Effect of range of attractive force

In this part, r_a, the parameter controlling the cut-off radius of attractive forces between two species is investigated to observe its influence on the macroscopic behaviour. The flow curves for r_a from 1.1 to 1.32 are shown in Figure 15. For the case that $r_a = 1.1$, 1.2, a small value of attractive cut-off radius, corresponds to insufficient bonds needed to form the microstructure network. Hence the fluid behaves such a Newtonian-like fluid. It can be seen from the Figure 15, the fluid behaves more viscous at small shear rate for a larger attractive cut-off radius. This is understandable as a larger cut-off radius for attractive force means a larger effective zone, the $DPD^{(b)}$ particles can attract more neighboring $DPD^{(a)}$ particles, therefore increasing numbers of bonds, making the fluid harder to flow. This would make yield stress a higher value, as a larger stress is needed to break these bonds in order to make the fluid start flowing. The plastic viscosity is also increased due to the fact that the particulate network keeps growing which results in more resistant to the flow. However, it should

be noted that if r_a is increased too large (e.g. $r_a/r_r \geq 1.3$ for $\phi = 0.2$ and DPD parameters listed in Table 2), some bulky clusters may be formed which make the system non-homogeneous.

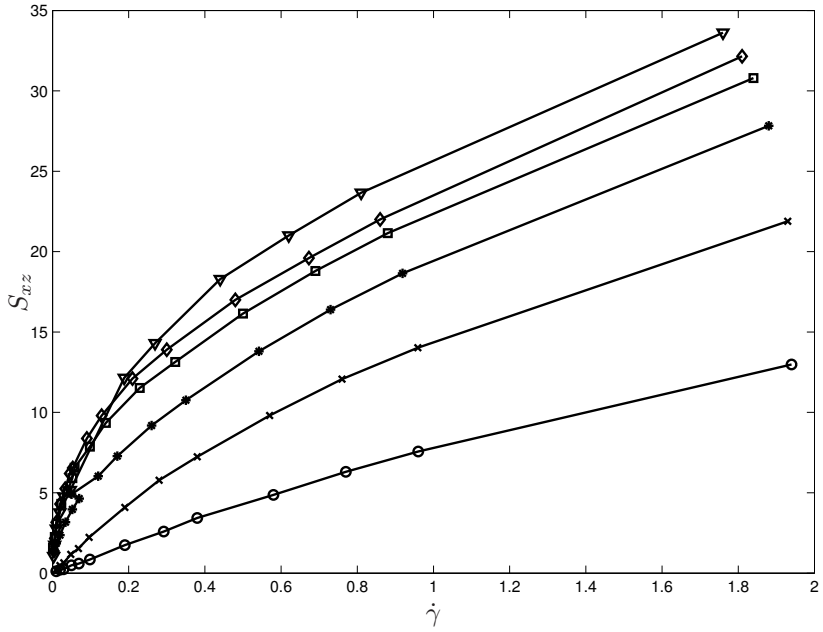

Figure 15: Couette flow: Non-linear shear stress - shear rate behaviour at different values of $r_a = \{1.32, 1.3, 1.28, 1.26, 1.2, 1.1\}$, from top to bottom.

6.1.2. Effect of concentration ratio, ϕ

The concentration ϕ is increased from 0.05 to 0.2 and the result is presented on Figure 16. As expected, at low concentration of $DPD^{(b)}$ particles, the fluid behaves like a Newtonian fluid as the connections between two species are not sufficient to create a particulate network. Again, at larger concentrations of $DPD^{(b)}$ particles, the fluid behaves more like a very high viscous material at small shear rate, thus is leaning towards a Bingham plastic material. Due to the increasing amounts of interaction among particles, more bonds are formed, thus hinder the flow. This structure also results in larger stress needed to cause

the material to shear, i.e., larger stress for flow to start, thus a higher yield stress trend is observed. It is observed that if ϕ is roughly larger than 0.2 with $r_a = 1.3$ the material become too viscous to have a proper flow.

However, one may expected that a smaller r_a allows a larger range of ϕ available for the model. In an attempt to verify this, some numerical experiments are carried out for $\phi = 0.28$ and three values of r_a including $\{1.23, 1.24, 1.25\}$ (smaller than 1.3). From Figure 17, at $r_a = 1.25$, the fluid shows a clear non-linear behaviour from the shape of the flow curve, and resembles a pseudo-yield stress material. Thus with a concentration $\phi = 0.28$, a decreasing of r_a roughly from 1.3 to 1.25 is needed to obtain a proper flow. It can be seen that with material of DPD parameters $\phi = 0.28, r_a = 1.25$, the shear stress versus shear rate curve exhibits clearer yield stress behaviour than that of $\phi = 0.2, r_a = 1.3$ (lower concentration but higher attractive cut-off radius).

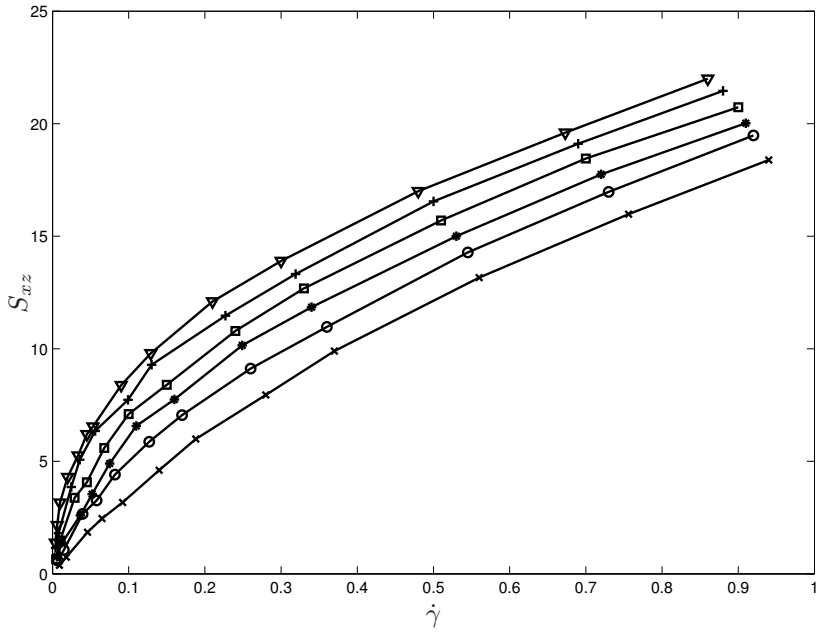

Figure 16: Couette flow: Non-linear shear stress - shear rate behaviour at different values of $\phi = \{0.200, 0.175, 0.150, 0.125, 0.100, 0.050\}$, from top to bottom.

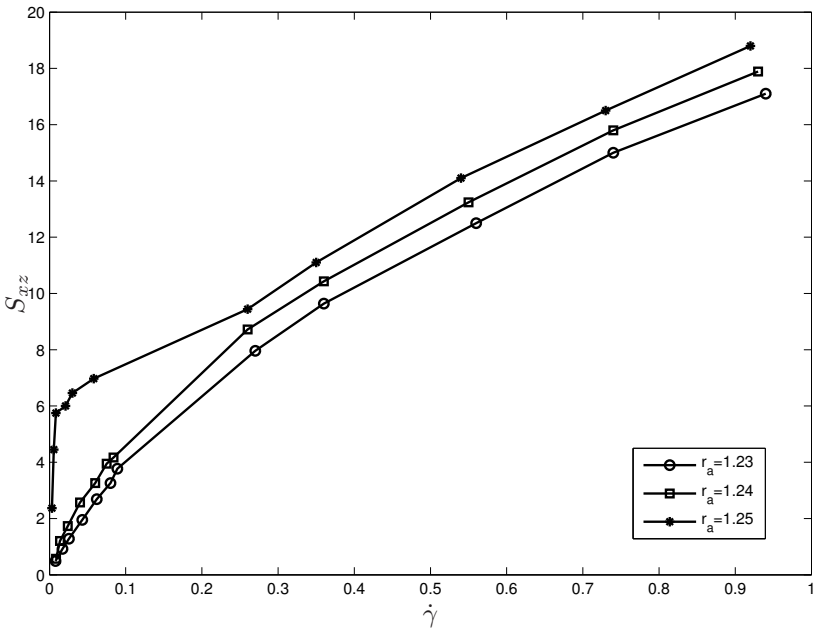

Figure 17: Couette flow: Non-linear shear stress - shear rate behaviour of $\phi = \{0.28\}$ and $r_a = \{1.23, 1.24, 1.25\}$.

6.2. Constants structure curves

In this section we investigate the transient response of the ILDP fluid, shown in Figure 18, where an overshoot in the shear stress can be observed. It is noted that there is no overshoot when the attractive force component is set to zero (i.e., when $B = 0$). The ILDP yield stress fluid is also thixotropic and can be represented by a family of constant structure (CS) curves, in the same manner as described by [9] and [34].

To measure the CS curves, we carry out a step-change in a shear rate experiment (Figure 19), as suggested by [34]. It is known that each reference shear rate has one structure level corresponding to a CS curve; therefore, the test is carried out by choosing one reference shear rate and then increase or decrease around this reference value. For example, the ILDP fluid is placed between two

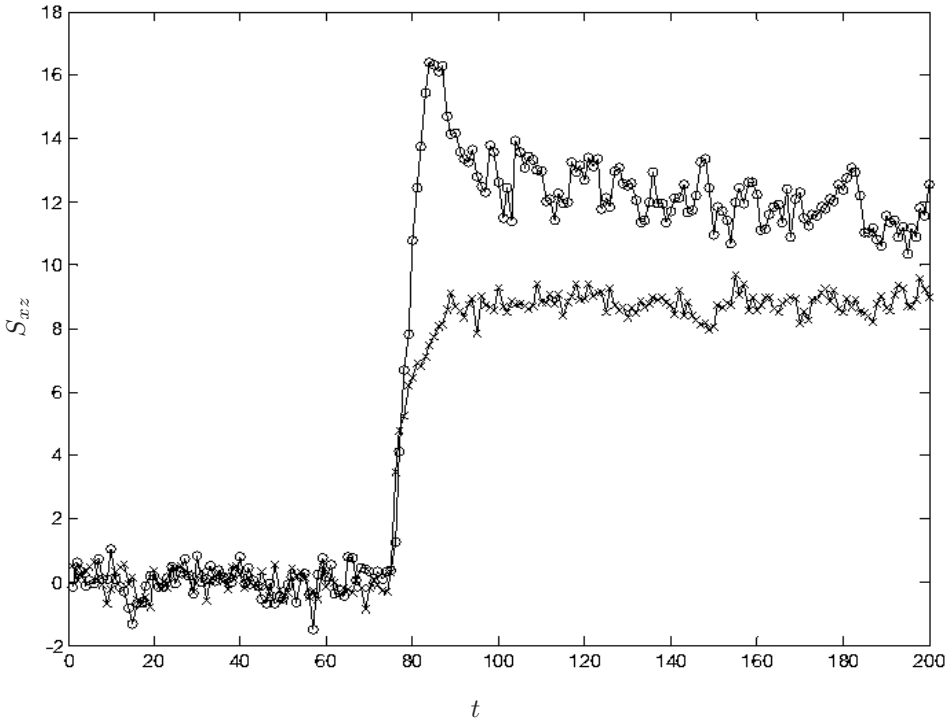

Figure 18: Thyxotropic behaviour: Time response of ILDP fluid ($-\circ$) and that of a DPD Newtonian fluid ($-\times$) in a simple shear flow with a constant shear rate $\dot{\gamma} = 0.3$.

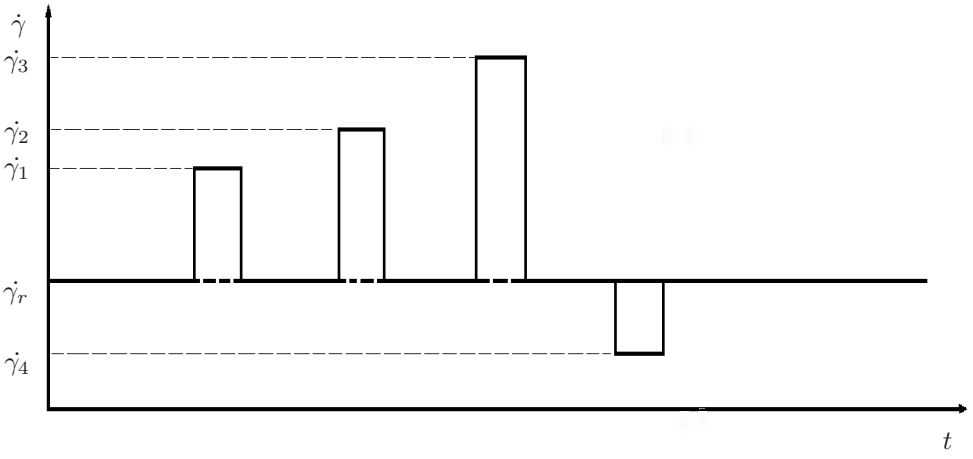

Figure 19: Thyxotropic behaviour: Shear rate experiments with step-change to obtain the family of constant structure curves.

parallel plates and subjected to a reference shear rate $\dot{\gamma} = \dot{\gamma_r}$ until the equilibrium state is reached. A higher shear rate $\dot{\gamma} = \dot{\gamma_1}$ is then applied and the peak value of shear stress S_1 is noted before $\dot{\gamma}$ is set back to $\dot{\gamma_r}$. The same procedures are carried out with $\dot{\gamma} = \{\dot{\gamma_2}, \dot{\gamma_3}, \ldots, \dot{\gamma_n}\}$ and $S = \{S_2, S_3, \ldots, S_n\}$ are noted. The CS curve for the shear rate $\dot{\gamma_r}$ is the plot of S versus $\dot{\gamma}$. In this report, we repeat this procedure for three reference shear rates $\dot{\gamma_r} = \{0.05, 0.36, 1.91\}$ and then plotted the set of CS curves. To quantify the time dependent rheological behaviour, the non-dimensional structure parameter λ as introduced in [9] is adopted. Here the maximum value of the degree of structure λ_0 is set to one (i.e., fully structured); the value of λ_e of each reference shear rate is determined from Eq.13. To construct the CS curves in Toorman's model (16), there are four parameters S_0, μ_∞, c and β are needed. By fitting, one can find these four parameters $S_0 = 5.13, \mu_\infty = 12.16, c = 73.57$ and $\beta = 60.57$ from the Bingham flow curve with a high shear viscosity of 11.66 and a yield stress of 6.72 (which corresponds to a DPD fluid having parameters listed in Table 2 and $r_a = 1.24, \phi = 0.4$). The fixed value of λ_i on a CS curve is to be identified as λ_E at the crossover point between this CS and the EF curves. A substitution of those values ($S_0, \mu_\infty, c, \beta$) and λ_i of each CS curve in Eq.16 give a family of CS curves.

In Figure 20, a comparison of the DPD data and CS curves obtained from Toorman's model is shown. It can be seen that the ILDP fluid responds in a similar manner to Toorman's model for a structure dependent thixotropic fluid.

6.3. Poiseuille flow

In this part, we explore ILDP fluid in Poiseuille flow. As shown in Figure 21, an ILDP fluid is placed between two parallel plates under a body force field $\mathbf{g} = (g_x, 0, 0)$ to simulate Poiseuille flow (in the $x-$direction). Periodic boundary conditions are applied to fluid boundaries in the $x-$ and $y-$directions. Velocity component in $x-$direction, u_x, is plotted versus $z-$coordinate to construct the velocity profile. z_0 is the transition line at which the material yields.

We consider the same ILDP fluid with parameters tabulated in (Table 2).

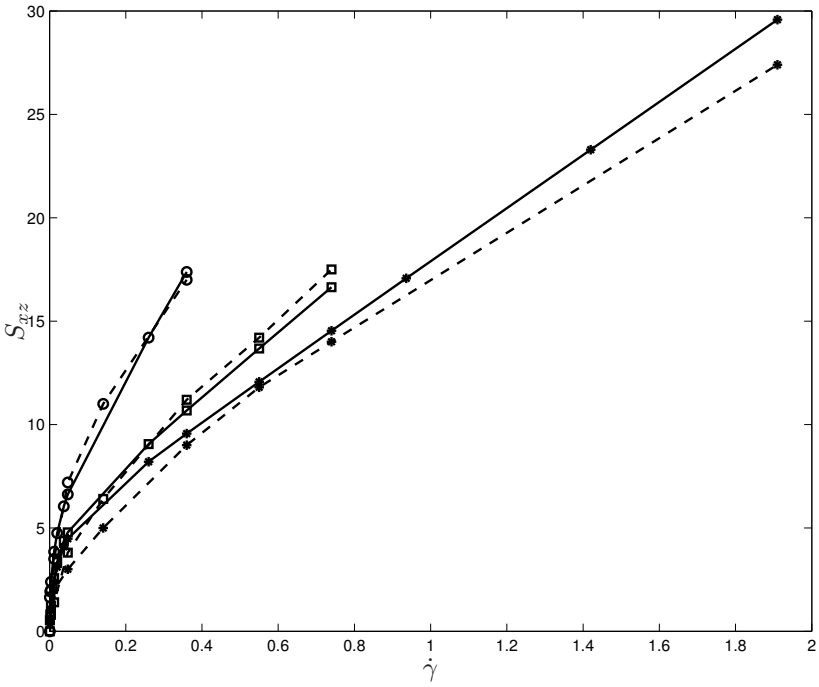

Figure 20: Shear stress plotted as a function of shear rate: constant structure curves (CSC). Dash line: constant structure curves obtained from DPD data for reference shear rates $\dot{\gamma}_r = 0.05(-\circ), 0.36(-\square), 1.91(-*)$ (from top to bottom); solid line: Toorman's model.

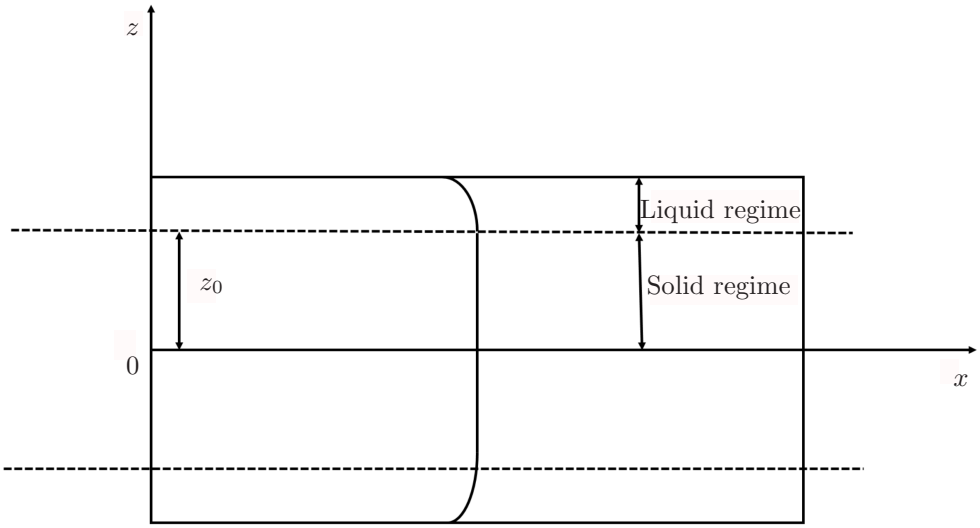

Figure 21: Poiseuille flow between two parallel plates: unyield and yield regions for velocity profile u_x along $z-$direction.

Figure 22 provides the plot of u_x with respect to the applied body force $g_x = 0.3$. As expected, the velocity profile of ILDP fluid (Figure 22b) is no longer parabolic as that of DPD-Newtonian fluid ($\mathbf{f}^{Ca} = 0$, Figure 22a). The plugged flow region near the centre is clearly visible - in this region the shear rate is low, consequentially the applied stress is smaller than the yield tress S_0 leading to a plugged flow.

Comparison velocity profile to the analytic solution of Bingham model: with a body force of $g_x = \{0.1, 0.2, 0.3, 0.4, 0.5\}$, the phase transition point z_0 changes from solid to liquid regime. With larger body force, the velocity profile becomes more parabolic, with a smaller plugged (no-yield) zone. At large enough pressure gradient, the plugged zone reduces to zero indicating that the applied stresses are large enough to break all particulate structures. We note that the analytical solution of non-dimensional Bingham model can be written

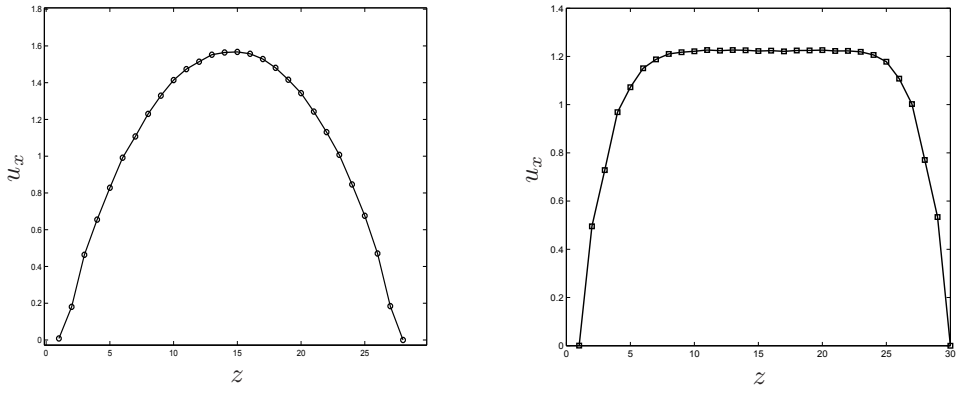

Figure 22: Poiseuille flow: Average velocity u_x : (a) DPD-Newtonian fluid$-\circ$ ($\mathbf{f}^{Ca} = 0$) - (b) ILDP fluid$-\square$ (Table 2, $\phi = 0.2$).

as [38], [5]

$$u_x = \frac{1}{2} g_x (H^2 - z^2) - Bn(H - z) \quad z_0 < z < H \tag{28}$$

$$u_x = \frac{1}{2} g_x (H - z_0)^2 \quad 0 < z < z_0, \tag{29}$$

The phase transition point is determined by $z_0 = Bn/g_x$ (Bn the Bingham number; g_x the non-dimensional pressure gradient). It can be seen that the line $z = z_0$ is the threshold between the pre- and post-yield zones and it can be determined simply by tracking the point when the applied shear stresses larger than yield stress value S_0. For example in Figure 23, the ratio $|Sxz/S_0|$ is larger than one at position $z = 0.13$, one can consider the line $z_c = 0.13$ the phase transition line. Based on the analytical solution at the plateau zone, one can determine the value z_0 from the plug zone:

$$\frac{u_x}{g_x} = \frac{1}{2}(H - z_0)^2. \tag{30}$$

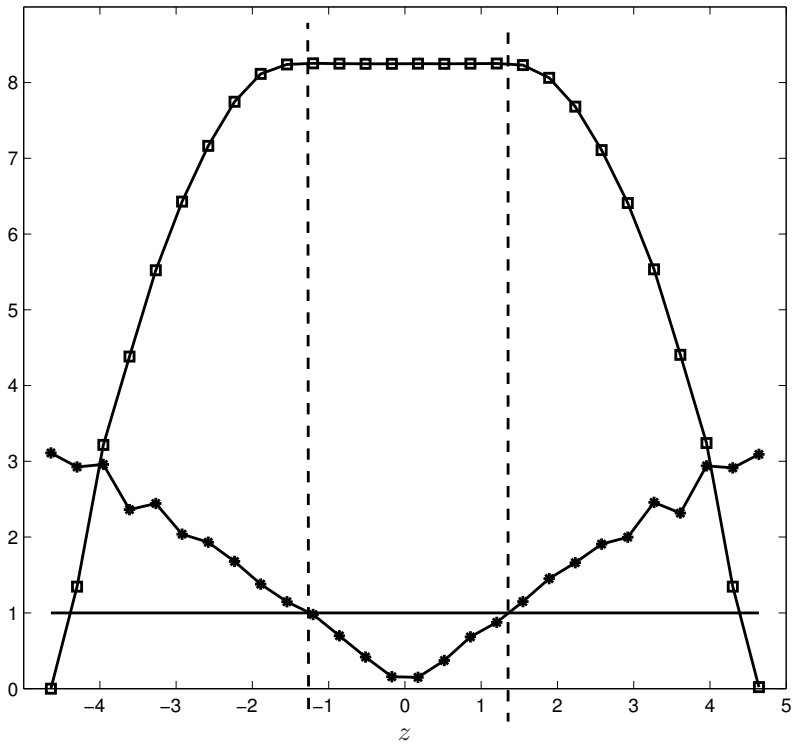

Figure 23: Poiseuille flow: Average velocity u_x $(-\square)$ and variation of $|Sxz/S_0|$ $(-*)$across the channel the $x-$component of applied body force 0.8.

This equation can be rewritten as

$$z_0 = H - \sqrt{2\frac{u_x}{g_x}}. \tag{31}$$

The maximum value of velocity u_x, the $x-$component of body force g_x and the yield line z_0, calculated from Eq.31, are listed in Table 4. The non-dimensional velocity profiles of ILDP fluid and the analytical solution for Bingham number $Bn = 0.2, 0.22, 0.25, 0.29, 0.34$ are shown in Figure 24. It can be seen that the ILDP results are comparable to those of analytical solutions. However, it should be noted that at the transition zones, the ILDP fluid exhibits a "softer" transition than that of a Bingham fluid (i.e., representing a transition here between high and low viscous flow regimes rather than the solid to liquid regimes transition in a truly yield stress fluid).

Table 4: DPD Poiseuille flow: maximum velocities with respect to $g_x = \{0.2, 0.3, 0.4, 0.5, 0.6\}$ and transition line z_0.

g_x	u_x	z_0
0.2	1.2	0.34
0.3	2.22	0.29
0.4	3.13	0.25
0.5	3.80	0.22
0.6	4.30	0.20

7. Concluding Remarks

In the present study, the DPD method has been used as a bottom-up approach to obtain the desired macroscopic properties for a yield-stress and thixotropic material. We propose a simple way to construct a particulate structure network to mimic the natural processes in concentrated cohesive mixtures. The DPD model comprises of two DPD species with different conservative forces, one with only repulsive forces (between the same species) and the other with short range repulsive and long-range attractive forces (between different species) - we call this DPD fluid the Indirect Linkage Dissipative Particle (ILDP) fluid.

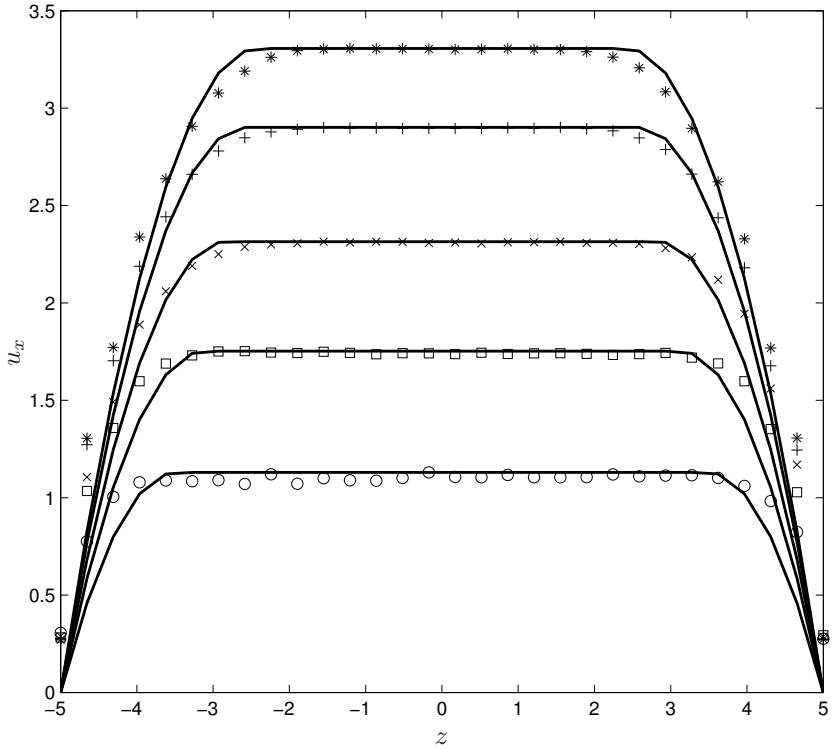

Figure 24: Poiseuille flow: Non-dimensional velocity profiles ($*$, $+$, $\times$, $\square$, $\circ$) with respect to $Bn = 0.2, 0.22, 0.25, 0.29, 0.34$ from top to bottom and the analytical steady state solutions of Bingham fluids ($-$).

The constitutive framework is fully specified with the microstructure that goes into the description of the DPD model. In particular, the numerical results demonstrate that

- The indirect linkage between $DPD^{(b)}$ particles insures that the uniform distribution of two DPD species over the computational domains;
- An ILDP microstructure network is formed and ruptured under a certain applied stress and then recovers when the applied stress level sufficiently reduces;
- Yield stress and shear thinning effects are the consequences of the flocculation and break up of the microstructures;
- The shear stress/shear rate curves are shifted up (i.e., increasing Papanastasiou's parameter n) with decreasing the kinetic energy of ILDP fluid.

The present model is able to produce nonlinear and thixotropy between shear stress and shear rate in viscometric flow that have been observed, or predicted by continuum methods. The ILDP velocity profile in Poiseuille flow is similar to analytical solution obtained with the Bingham's model. The model also produces the expected CS curves from high shear to low shear and vice versa flows, in qualitative agreement with Toorman's model. More detailed studies on the transient flows of thixotropic fluid with the ILDP model should be a welcome contribution, in particular in the area of highly concentrated and cohesive suspension mixtures.

The advantage of the DPD approach is that the multiphase properties of the system are reconstructed, without any reference to a particular constitutive equation. However, DPD model has many parameters to control such as conservative force coefficients including repulsive and attractive forces, random force and dissipative force coefficients, the Boltzmann temperature of the system, the ratio of $DPD^{(a)}$ and $DPD^{(b)}$ particles. A set of "standard" parameters have been well investigated, however. Another important parameter in addition to

the DPD parameter is concentration of one phase. Different from top-down approaches where macroscopic properties (e.g., viscosity, yield stress) are inputs which are obtained from physical experiments, the DPD fluid properties are the results of microstructure interactions, and the need of numerical experiments to determine a proper set of parameters.

The reported study was restricted to viscometric flows. For non-viscometric problems (e.g., contraction-expansion flows), compressibility effects may be present, which may effectively controlled by reducing DPD mass [19]).

Acknowledgement

The work is supported by an SMI grant SMI-2015-OF-08. The support is gratefully acknowledged.

References

[1] P. Coussot, A. Leonov, J. Piau, Rheology of concentrated dispersed systems in a low molecular weight matrix, Journal of Non-Newtonian Fluid Mechanics 46 (2) (1993) 179 – 217. doi:http://dx.doi.org/10.1016/0377-0257(93)85046-D.

[2] D. Bonn, J. Paredes, M. M. Denn, L. Berthier, T. Divoux, S. Manneville, Yield stress materials in soft condensed matter, arXiv:1502.05281.

[3] E. C. Bingham, Fluidity and Plasticity, McGraw-Hill, New York, 1922.

[4] T. C. Papanastasiou, Flows of materials with yield, Journal of Rheology 31 (5) (1987) 385–404. doi:http://dx.doi.org/10.1122/1.549926.

[5] R. R. Huilgol, Fluid Mechanics of Viscoplasticity, Springer-Verlag, Berlin Heidelberg, 2015.

[6] E. Mitsoulis, Flows of viscoplastic materials: models and computations, in: In Rheology Reviews 2007, 2007.

[7] F. Moore, The rheology of ceramic slips and bodies, Transactions and Journal of the British Ceramic Society 58 (1959) 470.

[8] P. Coussot, Q. D. Nguyen, H. T. Huynh, D. Bonn, Avalanche behavior in yield stress fluids, Physical Review Letters 88 (2002) 175501. doi:10.1103/PhysRevLett.88.175501.

[9] E. A. Toorman, Modelling the thixotropic behaviour of dense cohesive sediment suspensions, Rheologica Acta 36 (1) (1997) 56–65. doi:10.1007/BF00366724.

[10] P. J. Hoogerbrugge, J. M. V. A. Koelman, Simulating microscopic hydrodynamic phenomina with dissipative particle dynamics., Europhysics Letters 19 (1992) 155–160.

[11] L. D. Landau, E. M. Lifshitz, Fluid Mechanics, translated by J. B. Sykes and W. H. Reid, Pergamon Press, New York, 1959.

[12] P. Español, Hydrodynamics from dissipative particle dynamics, Physical Review E 52 (1995) 1734–1742. doi:10.1103/PhysRevE.52.1734.

[13] Phan-Thien, Understanding Viscoelasticity An Introduction to Rheology, Springer, 2013.

[14] P. Español, M. Revenga, Smoothed dissipative particle dynamics, Physical Review E 67 (2003) 026705. doi:10.1103/PhysRevE.67.026705.

[15] J. Koelman, P. Hoogerbrugge, Dynamic simulation of hard sphere suspensions under steady shear., Europhysics Letters 21 (1993) 363–368.

[16] S. Chen, N. Phan-Thien, B. C. Khoo, X. J. Fan, Flow around spheres by dissipative particle dynamics, Physics of Fluids 18 (2006) 103605.

[17] W. Pan, B. Caswell, G. E. Karniadakis, Rheology, microstructure and migration in brownian colloidal suspensions, Langmuir 26 (2009) 133–142.

[18] X. Bian, S. Litvinov, R. Qian, M. Ellero, N. A. Adams, Multiscale modeling of particle in suspension with smoothed dissipative particle dynamics, Physics of Fluids 24 (1). doi:http://dx.doi.org/10.1063/1.3676244.

[19] N. Mai-Duy, D. Pan, N. Phan-Thien, B. C. Khoo, Dissipative particle dynamics modeling of low reynolds number incompressible flows, Journal of Rheology 57 (2) (2013) 585–604. doi:http://dx.doi.org/10.1122/1.4789444.

[20] N. Phan-Thien, N. Mai-Duy, B. C. Khoo, A spring model for suspended particles in dissipative particle dynamics, Journal of Rheology 58 (4) (2014) 839–867. doi:http://dx.doi.org/10.1122/1.4874679.

[21] E. S. Boek, P. V. Coveney, H. N. W. Lekkerkerker, P. van der Schoot, Simulating the rheology of dense colloidal suspensions using dissipative particle dynamics, Physical Review E 55 (1997) 3124–3133. doi:10.1103/PhysRevE.55.3124.

[22] A. Vázquez-Quesada, M. Ellero, P. Español, Smoothed particle hydrodynamic model for viscoelastic fluids with thermal fluctuations, Physical Review E 79 (2009) 056707. doi:10.1103/PhysRevE.79.056707.

[23] W. Li, J. Ouyang, Q. Liu, An efficient dissipative particle dynamics-based algorithm for simulating ferromagnetic colloidal suspensions, ASME-Journal of Computational and Nonlinear Dynamics 11 (2) (2015) 024501–024501–6.

[24] A. Satoh, R. W. Chantrell, Application of the dissipative particle dynamics method to magnetic colloidal dispersions, Molecular Physics 104 (20-21) (2006) 3287–3302. arXiv:http://dx.doi.org/10.1080/00268970601094437, doi:10.1080/00268970601094437.

[25] C. Pastorino, A. G. Goicochea, Dissipative Particle Dynamics: A Method to Simulate Soft Matter Systems in Equilibrium and Under Flow, Springer International Publishing, Cham, 2015, pp. 51–79. doi:10.1007/978-3-319-11487-3_3.

[26] S. Litvinov, M. Ellero, X. Hu, N. A. Adams, Smoothed dissipative particle dynamics model for polymer molecules in suspension, Physical Review E 77 (2008) 066703. doi:10.1103/PhysRevE.77.066703.

[27] G. J. A. Sevink, J. G. E. M. Fraaije, Efficient solvent-free dissipative particle dynamics for lipid bilayers, Soft Matter 10 (2014) 5129–5146. doi:10.1039/C4SM00297K.

[28] X. Fan, N. Phan-Thien, S. Chen, X. Wu, T. Y. Ng, Simulating flow of dna

suspension using dissipative particle dynamics., Physics of Fluids 18 (2006) 063102(10).

[29] Y. Kong, C. Manke, W. Madden, A. Schlijper, Simulation of a confined polymer in solution using the dissipative particle dynamics method., International Journal of Thermophysics 15 (1994) 592–602.

[30] W. Pan, B. Caswell, G. E. Karniadakis, A low-dimensional model for the red blood cell, Soft Matter 6 (2010) 4366–4376. doi:10.1039/C0SM00183J.

[31] T. Ye, N. Phan-Thien, B. Khoo, C. Lim, Stretching and relaxation of malaria-infected red blood cells, Biophysical Journal 105 (5) (2013) 1103 – 1109. doi:http://dx.doi.org/10.1016/j.bpj.2013.07.008.

[32] C. Marsh, Theoretical Aspects of Dissipative Particle Dynamics, PhD Thesis, University of Oxford, 1998.

[33] J. H. Irving, J. G. Kirkwood, The statistical mechanical theory of transport processes. iv. the equations of hydrodynamics, The Journal of Chemical Physics 18 (6) (1950) 817–829. doi:http://dx.doi.org/10.1063/1.1747782.

[34] D. C.-H. Cheng, Yield stress: A time-dependent property and how to measure it, Rheologica Acta 25 (5) (1986) 542–554. doi:10.1007/BF01774406.

[35] M. Liu, P. Meakin, H. Huang, Dissipative particle dynamics with attractive and repulsive particle-particle interactions, Physics of Fluids 18 (1). doi:http://dx.doi.org/10.1063/1.2163366.

[36] M. Arienti, W. Pan, X. Li, G. Karniadakis, Many-body dissipative particle dynamics simulation of liquid/vapor and liquid/solid interactions, The Journal of Chemical Physics 134 (20). doi:http://dx.doi.org/10.1063/1.3590376.

[37] J. Steffe, Rheological Methods in Food Process Engineering, Freeman Press, 1996.
URL https://books.google.com.sg/books?id=LrrdONuST9kC

[38] H. Zhu, N. S. Martys, C. Ferraris, D. D. Kee, A numerical study of the flow of bingham-like fluids in two-dimensional vane and cylinder rheometers using a smoothed particle hydrodynamics (sph) based method, Journal of Non-Newtonian Fluid Mechanics 165 (78) (2010) 362 – 375. doi:http://dx.doi.org/10.1016/j.jnnfm.2010.01.012.